Compact differential gravimeter at the quantum projection-noise limit

Camille Janvier, Vincent Ménoret, Bruno Desruelle, Sébastien Merlet, Arnaud Landragin, Franck Pereira dos Santos

Compact differential gravimeter at the quantum projection-noise limit

Camille Janvier, * Vincent Ménoret, and Bruno Desruelle
iXblue Quantum Sensors, F-33400 Talence, France

Sébastien Merlet, Arnaud Landragin, and Franck Pereira dos Santos
LNE-SYRTE, Observatoire de Paris, Université PSL, CNRS, Sorbonne Université, F-75014 Paris, France

(Received 2 September 2021; revised 28 October 2021; accepted 10 January 2022; published 7 February 2022)

Atom interferometry offers new perspectives for geophysics and inertial sensing. We present the industrial prototype of a quantum-based instrument: a compact, transportable, differential quantum gravimeter capable of measuring simultaneously the absolute values of both gravitational acceleration g and its vertical gradient Γ_{zz}. While the sensitivity to g is competitive with the best industrial gravimeters, the sensitivity on Γ_{zz} reaches the limit set by quantum projection noise—leading to a long-term stability of 0.1 E ($1\,\mathrm{E} = 1 \times 10^{-9}\ \mathrm{s}^{-2}$). This dual-purpose instrument constitutes the industrial integration of cold atom sensors for practical applications. It paves the way for different applications in geophysics, civil engineering, and gravity-aided navigation, where accurate mapping of the gravitational field plays an important role.

DOI: 10.1103/PhysRevA.105.022801

I. INTRODUCTION

Absolute gravimeters are prominent tools in geophysics [1], providing an integrative estimation of the surrounding mass density by measuring the gravitational acceleration g to a very high precision. Transportable [2,3], field-deployable [4,5] commercial instruments, based on either "classical" or on "quantum technologies" are commonly used for gravity surveys by end users in geophysics. However, these instruments remain largely limited by vibration noise from the environment. Gravity gradiometers circumvent this issue by measuring a differential quantity that is fundamentally insensitive to vibrations. This has made them powerful tools for spaceborne [6], and airborne surveys—in the form of commercial grade relative gravity gradiometers for the latter [7,8]. However, these instruments intrinsically suffer from drifts and require calibration on a regular basis.

Atom interferometers (AIs) [9] offer new solutions to this issue. In the past 20 years, AIs have evolved from large, complex laboratory research experiments [10–14], to compact instruments [3] that can be used outside the laboratory [5,15,16], or on moving platforms [17,18]. Not only have these quantum sensors demonstrated better performance than their classical counterparts [19,20], but they offer the possibility to perform simultaneous absolute measurements of the acceleration g and gradient Γ_{zz} due to gravity [21]. Combined, these two quantities provide an improved picture of the surrounding mass distribution [22,23]. Here, we report on the results obtained with such an instrument that combines state-of-the-art performances with a compact laser system and physical package allowing for its transport and quick installation. Results of its operation as a stationary device and a proof-of-principle experiment for mass weighing are presented.

*Corresponding author: camille.janvier@ixblue.com

II. HARDWARE

Compared to previous differential cold atom gradiometers, our instrument was designed from the very beginning as a compact, transportable differential gravimeter capable of performing long-term time-lapse measurements of both gravity and its vertical gravity gradient. It uses two vertically stacked AIs that measure gravity at two different heights while sharing the same interrogation laser. The architecture of our differential quantum gravimeter (DQG) is composed of two subsystems: a sensor head which contains the vacuum chamber where the measurement takes place, and an electronics and laser module that generates all the optical and electrical signals necessary for the control of the instrument (see Fig. 1). The laser system is based on frequency-doubled telecom fiber lasers and the same proven architecture that was presented in Ref. [3], but improved to offer better robustness, a threefold reduction of both volume—down to 0.1 m^3—and weight—down to 33 kg. In order to achieve the best performance possible while remaining compact and light enough to be transported without mechanical help, an innovative design was required for the sensor head. It is organized around a free-standing vacuum chamber that eliminates the need for a supporting structure. Moreover, all the trapping, cooling, and the state manipulation of the two rubidium (Rb) atom clouds is done simultaneously using a single laser beam and two pyramidal retroreflectors (see Methods). The simultaneous interrogation and detection of the two atom clouds also insures a maximal common mode rejection. The sensor head is 175 cm high and weighs 66 kg and, while running, the instrument has a power consumption of 200 W, making it suitable for field applications.

A measurement cycle lasts 1.08 s and is conducted as follows: Two ^{87}Rb atom clouds are trapped simultaneously using two magneto-optical traps (MOTs) in two pyramidal retroreflectors separated by 62.5 cm [24]. Each MOT is loaded

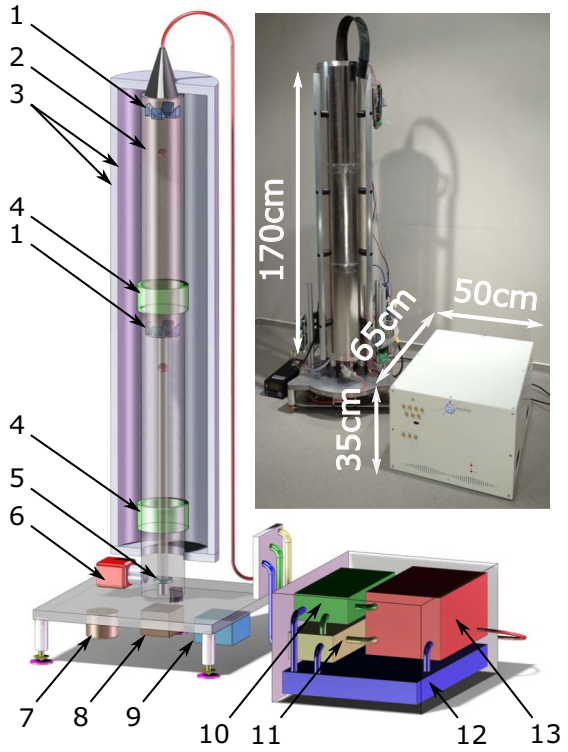

FIG. 1. Schematics and picture of the instrument: On the left the sensor head, on the right the electronic and laser system. (1) Top and bottom trapping pyramidal retroreflectors. (2) Vacuum chamber. (3) Inner, outer magnetic shields and coils. (4) Top and bottom detection areas. (5) Retroreflecting mirror on a tip-tilt piezo mount. (6) Ion pump. (7) Barometer. (8) Accelerometer. (9) Tiltmeter. (10) Embedded control computer. (11) rf synthesizer. (12) Power supply. (13) Laser optics. For a more thorough description of each subsystem, see Methods.

for 630 ms, after which the magnetic coils are switched off and the atoms further cooled down to 1.5 μK before being released. The magnetically sensitive atoms are removed from the cloud using magnetic substate selection. After this preparation, a Mach-Zehnder AI of duration $2T = 240$ ms is performed simultaneously on both clouds. The single laser beam produces the stimulated Raman transitions used as the atomic beam splitters [10,25,26] and is retroreflected on a common mirror placed on a piezo tip-tilt mount used to compensate for the Coriolis effect. Both are placed under ultrahigh vacuum in order to reduce biases from differential wave-front aberrations between the direct and the retroreflected Raman beams [27]. The phase ϕ of each interferometer includes the gravitational acceleration integrated over the respective trajectory of each atom cloud. It is extracted by evaluating the transition probability $P \propto \frac{1}{2}C\cos\phi$, where C is the interferometer contrast, from the ratio r of atoms detected in each internal state at the output of either interferometer. In order to be maximally sensitive to variations of this phase the interferometers are interrogated at midfringe and maintained in this configuration with a dual feedback loop on both the Raman frequency, and on a frequency jump on the Raman detuning for the second pulse of the interferometer, following Ref. [21]. The feedback on those quantities is then expressed in terms of gravity acceleration g, and its vertical gravity gradient Γ_{zz} using precisely known parameters of the interferometers (see Methods).

III. QPN-LIMITED GRADIENT MEASUREMENT

One of the main advantages of the differential gravimeter configuration is that a considerable amount of the noise to which gravimeters are sensitive to, is suppressed in the differential signal owing to efficient common-mode rejection. As a consequence, although the measurement of g is still sensitive to mirror vibrations, laser phase noise, and intensity fluctuations of the laser beam, the measurement of the gradient can become solely limited by the detection noise on the population ratios. This detection noise can be characterized by its Allan deviation σ_r, and is limited by quantum projection noise (QPN), as we show below. Note that although detection noise is commonly limited by QPN, only a few teams have reported the high-performance AI measurements at the QPN limit. Gauguet *et al.* [28] demonstrated such an operation with a fine characterization of the sensitivity of their device as a function of atom number, while Sorrentino *et al.* [29] mentioned it as the main contribution.

Detection noise is commonly decomposed in three kinds of contributions to σ_r, with different scalings with respect to the atom number N_{at}: $1/N_{\mathrm{at}}$, $1/\sqrt{N_{\mathrm{at}}}$, or independent of N_{at} [30,31]. The first contribution is dominated by technical noise such as shot noise in the electronics or stray light fluctuations. The second is the quantum projection noise which is a manifestation of the probabilistic nature of the measurement of a quantum superposition. The third arises for instance from optical noise due to laser frequency and intensity fluctuations. In the following, we first assess detection noise independently of any interferometer by preparing a state superposition using a $\pi/2$ microwave pulse. The result of this measurement is shown Fig. 2(a). We observe that the detection noise decreases for both the top and bottom clouds with respect to the detected atom number. While technical noise dominates at low atom number with a higher contribution for the top cloud, this contribution becomes negligible above 5×10^4 atoms for both clouds. Above this number, the two data sets follow the same $1/\sqrt{N_{\mathrm{at}}}$ scaling—confirming that the detection noise is indeed limited by QPN. No trace of a noise floor is observed in these data.

To confirm that the gravity gradient measurement is limited by detection noise and therefore by QPN, we measure the differential gravity noise $\sigma_{\Gamma_{zz}}$ as a function of atom number. The SI unit of Γ_{zz} is s^{-2} but common practice is to use eotvos ($1\ \mathrm{E} = 1 \times 10^{-9}\ \mathrm{s}^{-2}$) for a more compact notation. This quantity is estimated from the difference between detection ratios obtained from the top and bottom interferometers while both are in phase and at midfringe. Respective contrasts were measured to be $C_{\mathrm{bottom}} = 0.53$ and $C_{\mathrm{top}} = 0.42$. The result is shown in Fig. 2(b). As for the detection noise, the differential gravity noise is limited by technical noise at low atom number. For atom numbers ranging from 2.5×10^4 to 2.5×10^5, $\sigma_{\Gamma_{zz}}$ is dominated by $1/\sqrt{N_{\mathrm{at}}}$ noise which is well modeled by QPN accounting for the respective contrasts of the interferometers. In this regard, both data sets are in agreement and decreasing as the square root of the atom number for approximately one

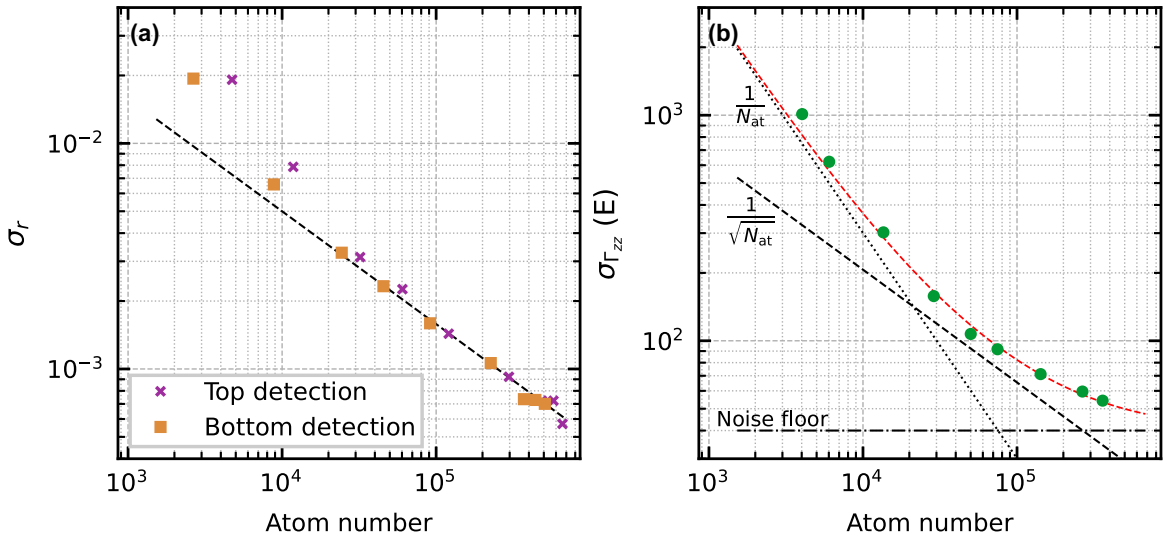

FIG. 2. Evolution of sensitivity with atom number: Detection (a) and gradient (b) noise as a function of atom number. The QPN model is shown as a dashed black line on both panels. On (b) it uses contrasts and parameters from the interferometers to estimate the effect of QPN on $\sigma_{\Gamma_{zz}}$. The full noise model (red dashed line) assumes a level of $1/N_{at}$ noise of 7×10^6 E atom$/\sqrt{\tau}$ (dotted line) and a noise floor of 40 E (dashed-dotted line).

decade—confirming that the gradient measurement is indeed QPN limited in the operating range below 2.5×10^5 atoms. Above this number, a fit to these data provides an estimated noise floor of 40 E. This is on the same level as the best sensitivity reported for an AI gravity gradiometer [32]. We attribute this noise floor to frequency noise on the Raman lasers (see Appendix 3 d) [33].

IV. STABILITY OF THE DUAL MEASUREMENT

Having characterized the short-term differential sensitivity, we now focus on long-term measurements. We present in Fig. 3 a 63-h-long differential gravity measurement obtained in laboratory conditions. We calculate gravity residuals $g - \tilde{g}$ by correcting the raw gravity signal for tilt [34], atmospheric pressure, and tidal fluctuations using a bespoke model for our measurement site [35]. The residuals reveal no significant drift which is confirmed by the total deviation that continuously decreases with averaging times down to 5 nm/ s^2 at 10000 s. From the slope of the total deviation we estimate the sensitivity of the gravity measurement at 750 nm s^{-2} $\tau^{-1/2}$. Unlike the gravity gradient measurement, this sensitivity is typically limited in our urban environment by acoustic and seismic noise due to anthropic activities. We mitigate these effects using an active vibration compensation system, which uses the signal of a classical accelerometer to act directly on the laser phase during the interferometer [36], as well as rubber pads placed under the apparatus to reduce high-frequency noise.

The total deviation of the gravity gradient measurement reaches 5 E after 100 s of integration which is compatible to the sensitivity measurements presented in Fig. 2. From this value and the sensitivity on the gravity measurement we estimate a lower bound for the common mode rejection ratio to be at least 24, and the total vibration rejection on the differential signal to be close to 230 owing to the active vibration compensation. The noise averages down with a hump around 1000 s, suggesting hourly fluctuations, down to 0.15 E at 110000 s. To our knowledge this is presently the best reported stability for a gravity gradiometer [29]. In terms of differential gravity measurement this represents a difference of less tha n 100 pm/ s^2 between the two interferometers. In terms of detectability, it corresponds to the gravity gradient anomaly generated by a 1-L cubical void in the ground 37 cm directly under the instrument (see Methods).

V. MASS WEIGHING EXPERIMENT

In order to further illustrate the potential for gravity surveys we perform a mass detection and weighing experiment. Compared to experiments that aim at accurately measuring the Newtonian constant of gravitation G [11–13], we chose application-relevant measurement parameters in terms of acquisition duration, size of the mass, and its position with respect to the instrument. The sensor head was lifted 16 cm above the ground on a table and a 147-kg lead mass was progressively moved below the table and then further away with an integration time of 1 h per position. The result is shown in Fig. 4, where the effect of the mass on the gradient is clearly resolved with a signal-to-noise ratio of ∼10, while the sensitivity on g is insufficient to resolve the anomaly with such a short averaging time. The experimental data are consistent with theoretical calculations, that take into account the geometry of the mass and the configuration of the interferometers (see Methods). Furthermore, in a more applicative approach, we can estimate the mass or density of the object from the data by fitting the gravity gradient anomaly using a least-squares adjustment of our theoretical model. We assume the size and dimension of the object to be known which is still relevant on an application standpoint. Indeed, in geophysics or civil engineering complementary methods such as ground-penetrating radar can provide this type of information. The fit estimate gives an estimated mass of 168(17) kg which is within a 2σ uncertainty of the actual mass. We note that the

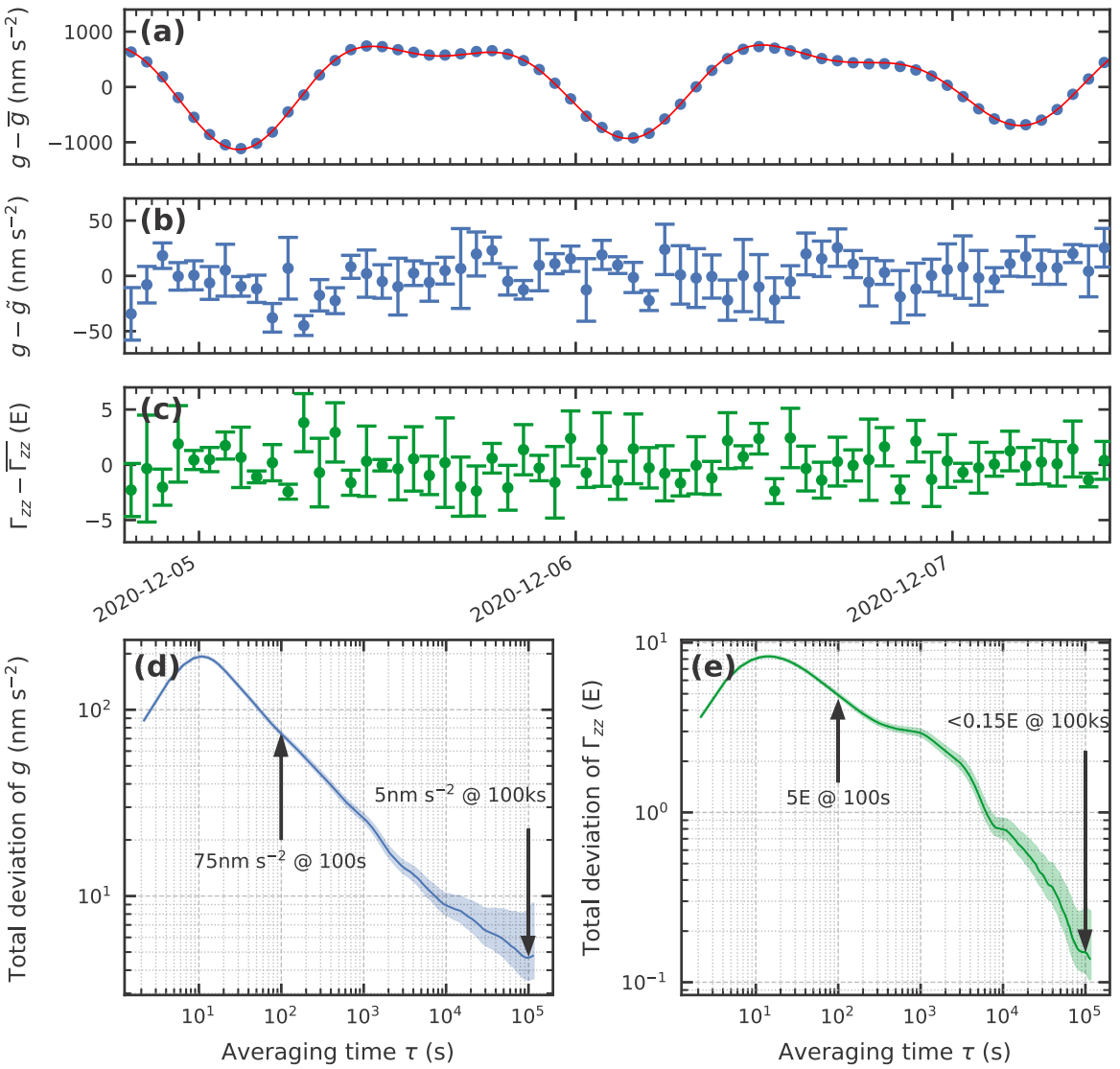

FIG. 3. Results of a 63-h dual measurement. (a) Measured g value averaged over 1 h superimposed with the local tide model (in red). (b) Gravity residuals $g - \tilde{g}$ averaged over 1h after correction for tilt, atmospheric pressure and tides. (c) Measured Γ_{zz} value averaged over 1 h. Average values for g and Γ_{zz} over the whole data set are 9805615664 nm/ s^2 and 2965.9 E. (d) and (e) Total deviation of the residuals of g and Γ_{zz}, respectively.

gravity signal is here too small to be used, but that for a larger mass it would be useful to better constrain the fit or improve its accuracy.

VI. CONCLUSION AND PERSPECTIVES

We have presented an AI gravity sensor that measures simultaneously both g and Γ_{zz} while being light enough to be handled by two people. Using an innovative design we were able to trap, manipulate, and detect simultaneously two atom clouds using a single laser beam. Not only did this result in a simple, light, and compact instrument, but also in an excellent common mode rejection, and made possible a QPN-limited measurement of the gravity gradient in a transportable AI sensor. We demonstrated state-of-the-art sensitivity and long-term performance of both gravitational acceleration and a vertical gravity gradient in a controlled laboratory environment. These performances have been subsequently used to demonstrate its potential for rapid detection and weighing of gravity anomalies such as subterranean masses or voids. This dual-purpose instrument is a prototype for a field-deployable device, yet it can already be employed for stationary geophysics measurements and indoor surveys. Because of their size, cost, limited uptime, or difficulty of operation, neither relative classical instruments nor previous cold atom gradiometers were suitable for these types of measurements. The dual measurement of g and Γ_{zz} opens possibilities for geophysics and reservoir monitoring. Furthermore, a full accuracy budget will establish the DQG as an absolute metrological instrument, while improvements in terms of ruggedization will lead to an operational instrument for outdoor use with practical field applications for geophysics and civil engineering.

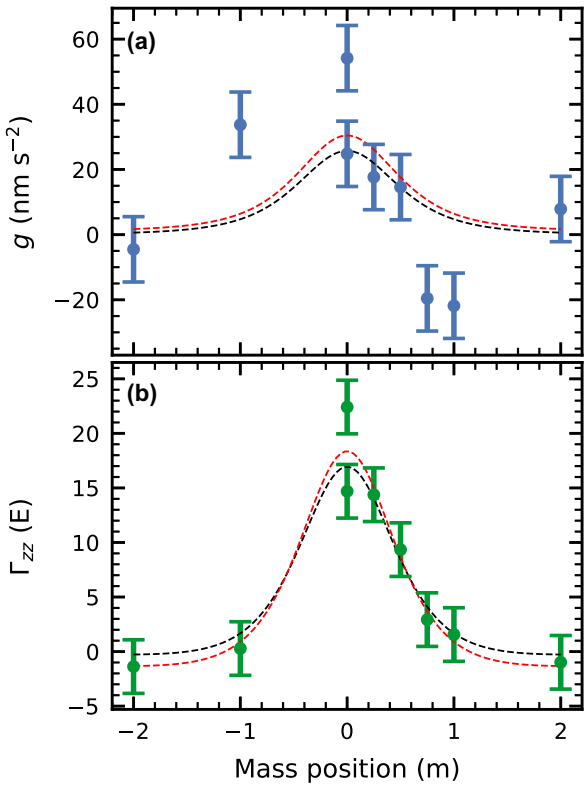

FIG. 4. Signals acquired by the DQG as a 147-kg lead mass is moved below the instrument with a 1-h integration duration per point. While the signal on g (a) is not resolved, the signal on Γ_{zz} (b) clearly reveals the effect of the mass. Error bars were estimated from the total deviation of a long measurement acquired the night after the experiment assuming a stationary noise. The model (black dashed lines) uses the physical parameters of the mass as well as the interferometer geometries to provide an accurate evaluation of the theoretical signal, where the only adjustable parameters are the offsets of the data (see Methods). The fit (red dashed lines) adjusts for density, gradient, and position offset on the gradient data.

ACKNOWLEDGMENTS

We would like to thank all the technical, scientific, and administrative personnel of iXblue for their work and support. We also thank Jackie Johnstone and Brynle Barrett for their valuable input on the paper. We acknowledge financial support by the ANR under Contract No. ANR-19-CE47-0003 GRADUS, and DGA under Contract No. 162906044 GRADIOM.

APPENDIX: MATERIAL AND METHODS

1. Hardware description of the instrument

a. Laser and electronics system

Two lasers are used to trap and manipulate the atoms in the sensor head. They are generated from frequency-doubled 1560-nm extended cavity diode lasers (ECDLs) and amplified by two erbium-doped fiber amplifiers (EDFAs). The two ECDLs are phase locked onto a master laser locked on a rubidium spectral line using a saturated absorption scheme. We use commercial periodically poled lithium niobate (PPLN) doubling crystals for the frequency doubling. An acousto-optical modulator (AOM) placed in the laser system generates the laser pulses. Except for the master laser, all frequencies in the instrument are generated from a 100-MHz oven-controlled crystal oscillator. Intermediate frequencies are synthesized from this reference using a 7-GHz phase-locked dielectric resonator oscillator (PLDRO) and direct digital synthesizers (DDSs). A measurement cycle is managed by an embedded computer in the laser system. This computer directly controls all the subsystems (including DDS, AOM, and EDFA power), gathers all the data from the sensor head (detection signals, tiltmeter, etc.), and performs all the calculations necessary to the dual tracking sequence. The measurement output and monitoring data are streamed by this on-board computer to a user interface computer used for remote control of the instrument and data collection.

b. Sensor head

The sensor head is organized around a free-standing titanium vacuum chamber and is about 175 cm high, 55 cm wide, and weighs 66 kg. In order to perform the differential measurement, two atom clouds are trapped in two different pyramidal retroreflectors separated by 62.5 cm. Commercial alkali-metal dispensers are used to produce a rubidium vapor in the vicinity of each trap. A notable difference with respect to the AQG design [3] is the placing of the mirror at the bottom of the vacuum chamber instead of the top in order to accommodate the piezo tip-tilt actuator used for Coriolis effect compensation [10,37]. The retroreflecting mirror that serves as an inertial reference frame for the measurement is fixed on top of this piezoactuator used to rotate the mirror during the free fall to compensate for the Coriolis effect. Both are placed under ultrahigh vacuum in order to reduce biases from differential wave-front aberrations between the direct and the retroreflected Raman beams [27]. Each atom cloud is detected in a dedicated detection zone consisting of two rows of photodiodes. The vacuum chamber is rigidly bolted to an aluminum tripod and supports two bias coils that generate a uniform magnetic field of 8 μT along the vertical axis, two layers of magnetic shielding, and the laser collimator placed on top of it. The ultrahigh vacuum inside the chamber is maintained using nonevaporable getters and an ion pump. All optical signals are amplified and digitized directly on the sensor head. A control board is responsible for the accelerometer signal acquisition and processing, involved in the active vibration compensation [3]. It also manages and synchronizes the sensor head subsystems and the communication with the laser system. A tiltmeter and a barometer complete the sensor instrumentation.

2. Dual tracking

Quantum gravimeters measure g from the phase of an atomic Mach-Zender interferometer by locking the Raman laser on its central fringe using an adjustable frequency chirp. To be able to track two interferometers at the same time, Caldani *et al.* [21] proposed to use an adjustment of the laser wave vector [38,39] to control the phase difference between the two interferometers. Adjusting both the frequency chirp and the wave vector gives access to g and Γ_{zz} simultaneously.

It also ensures a maximal common mode rejection [40], reduced sensitivity to contrast fluctuations, and optimizes the sensitivity of the instrument to phase variations of the interferometers by always measuring on the highest slope of the fringe. More importantly, this method eliminates the need for an independent measurement of the distance between the clouds, and is insensitive to its fluctuations.

In order to compensate for the effects of magnetic field and first-order light shifts, the effective wave vector of the Raman transition is reversed between successive measurement cycles—leading to two interleaved and independent dual-tracking feedback loops [41]. Finally, postcorrections are applied to the raw gravity signal to compensate for tides, atmospheric pressure [35], and tilts of the instrument [34]

Stability calculations presented in Fig. 3 use the total deviation, with error bars computed according to Ref. [42].

3. Detection noise and gradiometer sensitivity

a. Detection protocol

The population ratio between the outputs of the interferometers is measured as follows: A pulse of molasses light, red detuned from the $|F = 2\rangle \rightarrow |F' = 3\rangle$ cycling transition in ^{87}Rb, projects the measurement and stops the atoms in the $|F = 2\rangle$ state in front of a first row of photodiodes in each of the two detection areas, while the atoms in $|F = 1\rangle$ continue to fall. Once the $|F = 1\rangle$ atoms reach the second row of photodiodes, a resonant laser pulse is applied and the atomic fluorescence is collected by the photodiodes [43]. Finally a blow-away pulse (blue detuned from the cycling transition) is applied to remove all the remaining atoms from the detection area, and a second detection pulse is applied to measure and subtract any background light. The detection ratio is calculated from the fluorescence signal corrected by the detection offsets and crosstalks between detection rows. The same signals are converted to atom numbers [44], using a calibration factor that was estimated from the QPN measurement in Fig. 2(a) [31].

b. Atom number

The atom numbers in the sensitivity experiments were controlled by varying the time the laser was on during the MOT phase. Increasing this duration results in an increased atom number without changes to other experimental parameters. Crosstalks between two rows of photodiodes were measured for each configuration in order to account for the varying shape of the atom cloud.

c. Noise calculations

The detection noise in Fig. 2(a) was calculated as the one-sample Allan deviation of the detection ratio and plotted as a function of the respective atom number. For Fig. 2(b), the differential phase noise was measured at midfringe during an interferometer and was calculated as

$$\sigma_{\Gamma_{zz}} = \frac{2}{L k_{\text{eff}} T^2}\left(\frac{r_{\text{top}}}{C_{\text{top}}} - \frac{r_{\text{bottom}}}{C_{\text{bottom}}}\right), \tag{A1}$$

where L is the distance between atom clouds, k_{eff} the Raman effective wave vector, T the free evolution duration of the interferometer, and r_i and C_i are the population ratio and contrast of the interferometer $i =$ top, bottom.

d. Effect of laser frequency noise

Frequency noise has been shown to create phase noise on atom interferometers because of laser propagation delays [33,38]. Intuitively it is easy to see that noise on the frequency jump used to measure the differential phase will induce noise on this measurement. In our laser this frequency noise is mainly limited by electronic noise in our saturated absorption scheme. Following Ref. [33] and using an early characterization of the laser system, we found that the sensitivity limit set by the noise on the laser frequency is about 32 E per shot which is compatible with the 40-E floor observed in Fig. 2.

4. Setup and simulation of the mass detection

The sensor head of the DQG is placed on a small platform in order to be able to pass masses directly under it. The masses are moved under and away from it in steps. The distance between the top of the masses and the mirror is 31.5 cm. The mass is made of twenty 7.3 kg and $360 \times 90 \times 20\,\text{mm}^3$ lead bricks for easier manipulation. The assembled mass weighs 146.7 kg and measures $360 \times 360 \times 100\,\text{mm}^3$.

Because of its small size and density, the mass creates a gravitational attraction that is not linear along the atomic trajectories or between the two clouds. In order to have an accurate estimation of the effect of this mass on the measurement output of the DQG, we have to take into account these variations. To do so, we used a closed-form formula for prismatic masses [45] to calculate the gravitational pull of the mass along the unperturbed trajectories (i.e., assuming a constant gravitational acceleration) of the atomic wave packets, taking into account the different Raman recoil velocities in each arm of the interferometers. This force was then numerically integrated using the perturbative approach described in Ref. [46]. This calculation was performed for each interferometer and each effective wave-vector orientation. From this we extrapolated the theoretical anomaly both in g and Γ_{zz} as a function of the mass's position with respect to the instrument.

The same calculation was used for the estimation of the anomaly generated by a 1 L cubical void in the ground. The density of the cube was taken to be $2600\,\text{kg}\,\text{m}^{-3}$, directly under the instrument with its top surface 37 cm under the the sensor head. The anomaly was calculated to be 144 mE on the gravity gradient and $-0.24\,\text{nm}/\text{s}^2$ on gravitational acceleration.

[1] M. Van Camp, O. de Viron, A. Watlet, B. Meurers, O. Francis, and C. Caudron, Geophysics from terrestrial time-variable gravity measurements, Rev. Geophys. **55**, 938 (2017).

[2] T. M. Niebauer, G. S. Sasagawa, J. E. Faller, R. Hilt, and F. Klopping, A new generation of absolute gravimeters, Metrologia **32**, 159 (1995).

[3] V. Ménoret, P. Vermeulen, N. Le Moigne, S. Bonvalot, P. Bouyer, A. Landragin, and B. Desruelle, Gravity measurements below 10^{-9} g with a transportable absolute quantum gravimeter, Sci. Rep. **8**, 12300 (2018).

[4] J. Mäkinen, M. Sękowski, and J. Kryński, The use of the A10-020 gravimeter for the modernization of the finnish first order gravity network, Geoinf. Iss. **2**, 17 (2010).

[5] A.-K. Cooke, C. Champollion, and N. Le Moigne, First evaluation of an absolute quantum gravimeter (AQG#B01) for future field experiments, Geosci. Instrum. Method. Data Syst. **10**, 65 (2021).

[6] R. Rummel, W. Yi, and C. Stummer, GOCE gravitational gradiometry, J. Geod. **85**, 777 (2011).

[7] M. H. Dransfield, Airborne gravity gradiometry in the search for mineral deposits, in *Exploration in the New Millennium: Proceedings of the Fifth Decennial International Conference on Mineral Exploration*, edited by B. Milkereit (Decennial Mineral Exploration Conferences, Toronto, 2007), pp. 341–354.

[8] M. V. Moody, A superconducting gravity gradiometer for measurements from a moving vehicle, Rev. Sci. Instrum. **82**, 094501 (2011).

[9] R. Geiger, A. Landragin, S. Merlet, and F. Pereira Dos Santos, High-accuracy inertial measurements with cold-atom sensors, AVS Quantum Sci. **2**, 024702 (2020).

[10] A. Peters, K. Y. Chung, and S. Chu, High-precision gravity measurements using atom interferometry, Metrologia **38**, 25 (2001).

[11] J. B. Fixler, G. T. Foster, J. M. McGuirk, and M. A. Kasevich, Atom interferometer measurement of the Newtonian constant of gravity, Science **315**, 74 (2007).

[12] G. Rosi, F. Sorrentino, L. Cacciapuoti, M. Prevedelli, and G. M. Tino, Precision measurement of the Newtonian gravitational constant using cold atoms, Nature (London) **510**, 518 (2014).

[13] D.-K. Mao, X.-B. Deng, H.-Q. Luo, Y.-Y. Xu, M.-K. Zhou, X.-C. Duan, and Z.-K. Hu, A dual-magneto-optical-trap atom gravity gradiometer for determining the Newtonian gravitational constant, Rev. Sci. Instrum. **92**, 053202 (2021).

[14] P. Asenbaum, C. Overstreet, T. Kovachy, D. D. Brown, J. M. Hogan, and M. A. Kasevich, Phase Shift in an Atom Interferometer due to Spacetime Curvature Across its Wave Function, Phys. Rev. Lett. **118**, 183602 (2017).

[15] X. Wu, Gravity gradient survey with a mobile atom interferometer, Ph.D. thesis, Stanford University, 2009, https://web.stanford.edu/group/kasevich/cgi-bin/wordpress/wp-content/uploads/2012/09/WuThesis.pdf.

[16] X. Wu, Z. Pagel, B. S. Malek, T. H. Nguyen, F. Zi, D. S. Scheirer, and H. Müller, Gravity surveys using a mobile atom interferometer, Sci. Adv. **5**, eaax0800 (2019).

[17] B. Barrett, L. Antoni-Micollier, L. Chichet, B. Battelier, T. Lévèque, A. Landragin, and P. Bouyer, Dual matter-wave inertial sensors in weightlessness, Nat. Commun. **7**, 13786 (2016).

[18] Y. Bidel, N. Zahzam, A. Bresson, C. Blanchard, M. Cadoret, A. V. Olesen, and R. Forsberg, Absolute airborne gravimetry with a cold atom sensor, J. Geod. **94**, 20 (2020).

[19] P. Gillot, O. Francis, A. Landragin, F. Pereira Dos Santos, and S. Merlet, Stability comparison of two absolute gravimeters: Optical versus atomic interferometers, Metrologia **51**, L15 (2014).

[20] C. Freier, M. Hauth, V. Schkolnik, B. Leykauf, M. Schilling, H. Wziontek, H.-G. Scherneck, J. Müller, and A. Peters, Mobile quantum gravity sensor with unprecedented stability, J. Phys.: Conf. Ser. **723**, 012050 (2016).

[21] R. Caldani, K. X. Weng, S. Merlet, and F. Pereira Dos Santos, Simultaneous accurate determination of both gravity and its vertical gradient, Phys. Rev. A **99**, 033601 (2019).

[22] G. Pajot, O. de Viron, M. M. Diament, M. F. Lequentrec-Lalancette, and V. Mikhailov, Noise reduction through joint processing of gravity and gravity gradient data, Geophysics **73**, 123 (2008).

[23] Z. Ye, R. Tenzer, N. Sneeuw, L. Liu, and F. Wild-Pfeiffer, Generalized model for a Moho inversion from gravity and vertical gravity-gradient data, Geophys. J. Int. **207**, 111 (2016).

[24] B. Desruelle, P. Bouyer, and A. Landragin, Cold atom gravity gradiometer, U.S. Patent No. 9,134,450 (2014).

[25] C. J. Bordé, Atomic interferometry with internal state labelling, Phys. Lett. A **140**, 10 (1989).

[26] M. Kasevich and S. Chu, Atomic Interferometry Using Stimulated Raman Transitions, Phys. Rev. Lett. **67**, 181 (1991).

[27] A. Louchet-Chauvet, T. Farah, Q. Bodart, A. Clairon, A. Landragin, S. Merlet, and F. Pereira Dos Santos, The influence of transverse motion within an atomic gravimeter, New J. Phys. **13**, 065025 (2011).

[28] A. Gauguet, B. Canuel, T. Lévèque, W. Chaibi, and A. Landragin, Characterization and limits of a cold-atom Sagnac interferometer, Phys. Rev. A **80**, 063604 (2009).

[29] F. Sorrentino, Q. Bodart, L. Cacciapuoti, Y.-H. Lien, M. Prevedelli, G. Rosi, L. Salvi, and G. M. Tino, Sensitivity limits of a Raman atom interferometer as a gravity gradiometer, Phys. Rev. A **89**, 023607 (2014).

[30] W. M. Itano, J. C. Bergquist, J. J. Bollinger, J. M. Gilligan, D. J. Heinzen, F. L. Moore, M. G. Raizen, and D. J. Wineland, Quantum projection noise: Population fluctuations in two-level systems, Phys. Rev. A **47**, 3554 (1993).

[31] G. Santarelli, P. Laurent, P. Lemonde, A. Clairon, A. G. Mann, S. Chang, A. N. Luiten, and C. Salomon, Quantum Projection Noise in an Atomic Fountain: A High Stability Cesium Frequency Standard, Phys. Rev. Lett. **82**, 4619 (1999).

[32] S.-W. Chiow, J. Williams, and N. Yu, Noise reduction in differential phase extraction of dual atom interferometers using an active servo loop, Phys. Rev. A **93**, 013602 (2016).

[33] J. Le Gouët, P. Cheinet, J. Kim, D. Holleville, A. Clairon, A. Landragin, and F. Pereira Dos Santos, Influence of lasers propagation delay on the sensitivity of atom interferometers, Eur. Phys. J. D **44**, 419 (2007).

[34] T. M. Niebauer, T. Blitz, and A. Constantino, Off-level corrections for gravity meters, Metrologia **53**, 835 (2016).

[35] H. Wziontek, S. Bonvalot, R. Falk, G. Gabalda, J. Mäkinen, V. Pálinkás, A. Rülke, and L. Vitushkin, Status of the international gravity reference system and frame, J. Geod. **95**, 7 (2021).

[36] J. Lautier, L. Volodimer, T. Hardin, S. Merlet, M. Lours, F. Pereira Dos Santos, and A. Landragin, Hybridizing matter-wave and classical accelerometers, Appl. Phys. Lett. **105**, 144102 (2014).

[37] C. Freier, Atom interferometry at geodetic observatories, Ph.D. thesis, Humboldt-Universität zu Berlin, 2017, https://edoc.hu-berlin.de/handle/18452/18447.

[38] G. W. Biedermann, X. Wu, L. Deslauriers, S. Roy, C. Mahadeswaraswamy, and M. A. Kasevich, Testing gravity

with cold-atom interferometers, Phys. Rev. A **91**, 033629 (2015).

[39] A. Roura, Circumventing Heisenberg's Uncertainty Principle in Atom Interferometry Tests of the Equivalence Principle, Phys. Rev. Lett. **118**, 160401 (2017).

[40] F. Pereira Dos Santos, Differential phase extraction in an atom gradiometer, Phys. Rev. A **91**, 063615 (2015).

[41] D. S. Weiss, B. C. Young, and S. Chu, Precision measurement of hbar mCs based on photon recoil using laser-cooled atoms and atomic interferometry, Appl. Phys. B **59**, 217 (1994).

[42] D. Howe, The total deviation approach to long-term characterization of frequency stability, IEEE Trans. Ultrason. Ferroelectr. Freq. Control. **47**, 1102 (2000).

[43] J. M. McGuirk, G. T. Foster, J. B. Fixler, and M. A. Kasevich, Low-noise detection of ultracold atoms, Opt. Lett. **26**, 364 (2001).

[44] D. A. Steck, Rubidium 87 D Line Data (2019), https://steck.us/alkalidata/rubidium87numbers.pdf.

[45] X. Li and M. Chouteau, Three-dimensional gravity modeling in all space, in *SEG Technical Program Expanded Abstracts 1997* (Society of Exploration Geophysicists, Tulsa, 1997), pp. 474–477.

[46] G. D'Agostino, S. Merlet, A. Landragin, and F. Pereira Dos Santos, Perturbations of the local gravity field due to mass distribution on precise measuring instruments: A numerical method applied to a cold atom gravimeter, Metrologia **48**, 299 (2011).